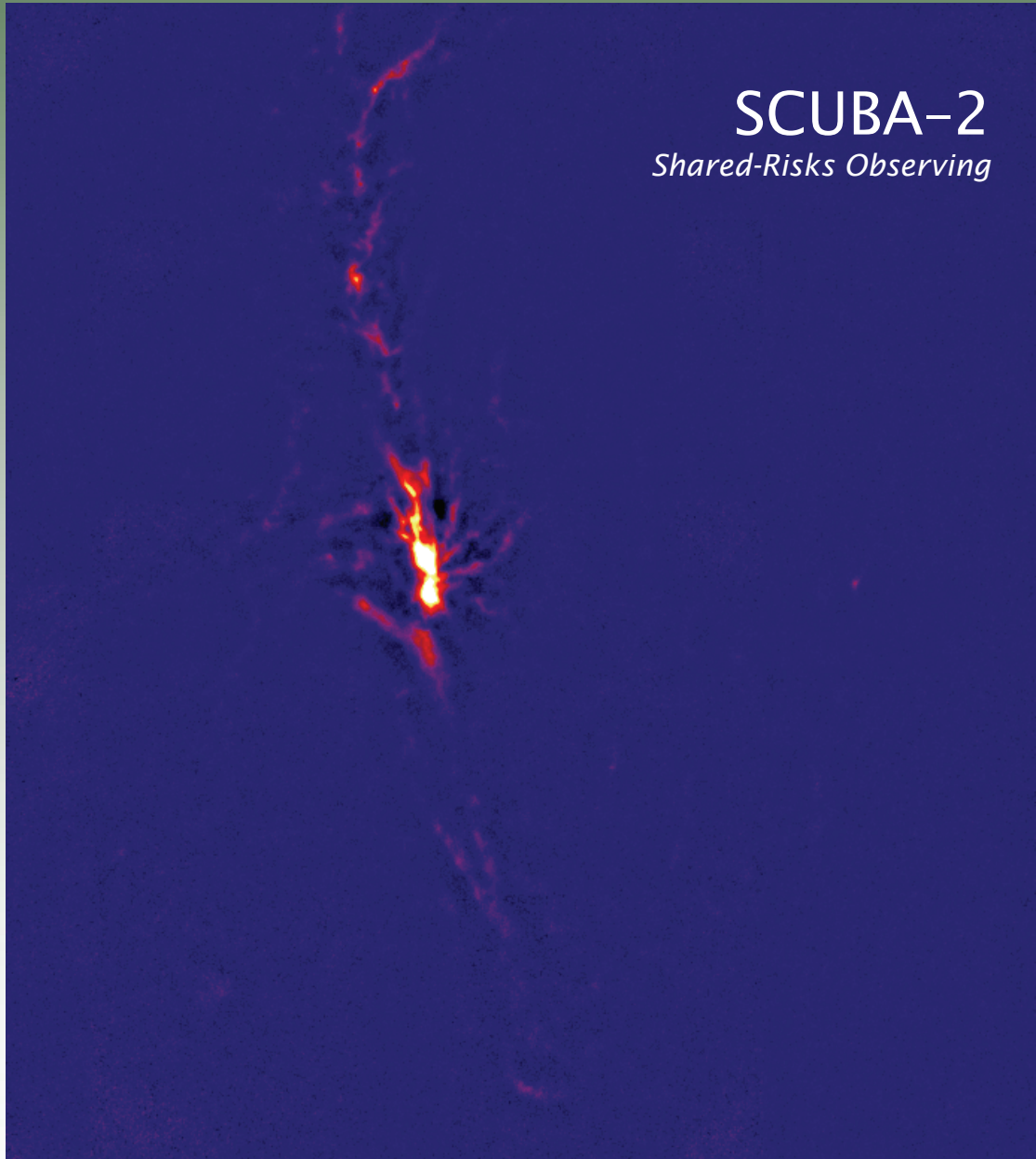




# JCMT NEWSLETTER

JAMES CLERK MAXWELL TELESCOPE

SPRING 2010 · #32





# In This Issue

JCMT Newsletter, James Clerk Maxwell Telescope, is published biannually and is edited by Antonio Chrysostomou and Jonathan Kemp.

ISSN 1351-5497. Copyright © 2010 by Science and Technology Facilities Council, Joint Astronomy Centre, Hilo, except where copyright retained by named individual article or image authors.

IN THIS ISSUE

From the Desk of the Director (Davis & Chrysostomou) ..... 3

## JCMT Science

Comparisons of Cold Dust, Polycyclic Aromatic Hydrocarbons, Molecular Gas, and Atomic Gas in NGC 2403 (Bendo) ..... 5

Probable Collision between a Comet and Saturn Two Centuries Ago (Cavalié, Billebaud, Dobrijevic, Hartogh, Fouchet, Lellouch, Encrenaz, Brillet, Schieven, & Wouterloot) ..... 8

## JCMT Operations

El Niño Effect on Mauna Kea (Tilanus) ..... 4

Automated Feature Extraction with HARP Data (Beaumont & Williams) ..... 10

The SCUBA-2 Shared-Risks Observing Campaign: An Overview (Chrysostomou) ..... 12

Observing Using Frequency Switching (Friberg) ..... 13

postal address  
James Clerk Maxwell Telescope  
Joint Astronomy Centre  
University Park  
660 North A`ohoku Place  
Hilo, Hawai`i 96720-2700  
USA  
telephone  
+1 (808) 961 - 3756  
facsimile  
+1 (808) 961 - 6516  
world wide web  
<http://www.jach.hawaii.edu/JCMT/>

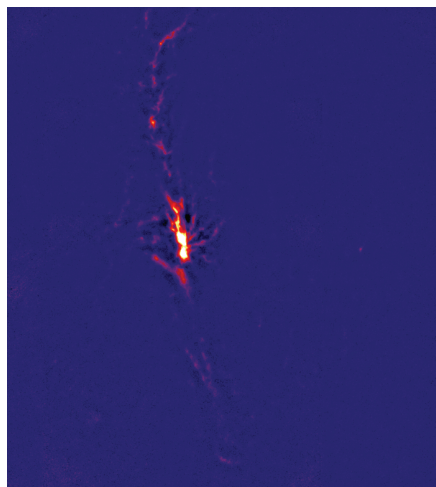
The Joint Astronomy Centre provides services and support to enable community and staff astronomers to undertake top-quality, front-line international-class research using the James Clerk Maxwell Telescope (JCMT); to develop the JCMT in order to maintain its position as the most advanced observatory of its kind in the world; to operate the United Kingdom Infrared Telescope (UKIRT) in a streamlined mode so as to expeditiously complete the world-leading UKIDSS programme, plus other programmes as resources permit; to operate both facilities in the most cost-effective and efficient manner on behalf of the funding agencies; and to be responsive to the changing needs of the contributing organisations.

The JCMT is supported by the United Kingdom's Science and Technology Facilities Council (STFC), the National Research Council Canada (NRC), and the Netherlands Organization for Scientific Research (NWO); it is overseen by the JCMT Board.

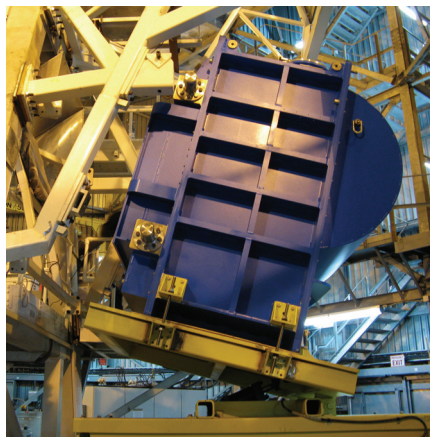
The JCMT is a member of the RadioNet consortium.



2



On the front cover: A SCUBA-2 450  $\mu$ m image of OMC-1 obtained during SCUBA-2 Shared-Risks Observing. (Also see article on page 12 of this issue.)



On the rear cover: SCUBA-2 mounted on the JCMT antenna. (Also see article on page 12 of this issue; image courtesy Jim Hoge/JAC.)

## From the Desk of the Director

Professor Gary Davis (*Director JCMT*) & Antonio Chrysostomou (*Associate Director JCMT*)



Gary Davis, Director JCMT

Readers of this column will be aware of the strategic importance of the SCUBA-2 instrument, not only for the JCMT Legacy Survey (JLS) in which a large fraction of the user community is involved, but also for the

future of the Observatory. It was therefore with great excitement and some trepidation that we commenced the challenging task of commissioning the instrument in late 2009 with the first two science-grade arrays, leading to a shared-risks observing campaign in early 2010. A separate article in this issue of the JCMT Newsletter describes the early science campaign in more detail.

The objective of this fast-track process providing early community access to SCUBA-2 was to demonstrate, by undertaking peer-reviewed science projects approved by the ITAC, that the instrument will fulfil its enormous scientific potential. As is only to be expected with an instrument of this complexity, the outcome was mixed. On the one hand, providing that the remaining six arrays perform at least as well as the first two, then the instrument will meet its performance specification. This is a powerful statement since the specification was based on a science case for the instrument which remains largely intact despite the years which have passed since it was developed. On the other hand, the astronomical performance of the instrument was not as good as we had hoped, and the sensitivity is currently limited by excess low-frequency noise in the system which manifests itself as large-scale features in the images. Dedicated technical teams have been set up to look

at this and other issues in detail. The remaining arrays are scheduled to arrive in Hawaii this summer, and commissioning of the instrument will take up the rest of the year and early 2011.

Forward planning processes have been taking place in two of the three partner countries. The Canadian Astronomical Society has launched the development of a Long-Range Plan, with extensive community consultation in early 2010 and a Plan scheduled for issue by the end of the year. In the UK, STFC conducted a prioritisation exercise during the second half of 2009, leading to an announcement in December of their science programme for the next five years. We were pleased to note that the JCMT, with SCUBA-2, was confirmed yet again (as in two previous Programmatic Reviews) as a must-do project for STFC. Regrettably, the JAC's other telescope did not fare so well in this process, and as a consequence UKIRT will adopt a "minimalist" operating mode at the end of 2010. This change of mode will have profound ramifications for the working culture of the JAC: in particular, rather than operating two telescopes of equal priority as has been the case for many years, the JCMT will in future be the JAC's primary telescope, with operational support for UKIRT only being provided subject to the JCMT's requirements.

Work on the JCMT Science Archive has continued apace, with several milestones achieved. The complete ACSIS catalogue of data has been re-reduced and the first multi-night reduced products are appearing for projects. Archive users should also have a different experience browsing the archive. Thumbnail images are presented which can be inspected in an Aladin viewer helping the user decide whether to download particular data files. These thumbnails are generated by the

ORAC-DR pipeline and are representative of the data product, *i.e.*, they give the integrated intensity image and the brightest spectrum from the cube. We have successfully transferred, ingested, reduced,

and delivered SCUBA-2 data. In fact, the relatively small period of time we have operated SCUBA-2 for over the autumn and winter months has had a profound and significant impact on the archive. As of April 2010, the archive as a whole (*i.e.*, over the whole history of the JCMT) occupied some 18.4 TB of disk space comprised of almost 1 million files. Of these, more than 13% are SCUBA-2 data files. We should take note here that this is with the instrument operating with just 2 of 8 science grade arrays and in non-continuous, commissioning mode. This gives us just a flavour of what is to come when we begin delivering a full science programme with the full complement of arrays and also demonstrates why we need a science archive.

In between on-sky commissioning and SCUBA-2 shared-risks observing we continue to deliver and support a continuing heterodyne science programme, both for the JLS and for projects allocated by the time allocation committees. The Nearby Galaxies Survey has now completed observing the HARP component of its survey, while the Gould Belt Survey and Spectral Legacy Survey are both close to completion. It is expected that these surveys will be complete by the end of Semester 10B.

The instrument suite and telescope have been performing well, with the

*(Director's Desk, continued on page 4)*



Antonio Chrysostomou, Associate Director JCMT





# El Niño Effect on Mauna Kea

Remo Tilanus (JCMT Head of Operations)

These plots show the amount of water vapor in the atmosphere above Mauna Kea for this year compared to the average for all years since 1989.

The plots show the percentage of nights per month with a 225-GHz opacity <0.05 (left panel) and <0.08

(right panel) since June last year (blue line), compared with the average (green line) since 1989. The effect of El Niño is especially pronounced in the left-hand plot which shows 'superior' weather conditions. It suggests that conditions have returned to average since the end of

March. The right-hand plot also includes 'good' weather: it shows a broader envelope and a lingering effect of El Niño. However, note that individual years typically can vary considerably from the average. ●

Nightly 225-GHz Opacity Mauna Kea < 0.05

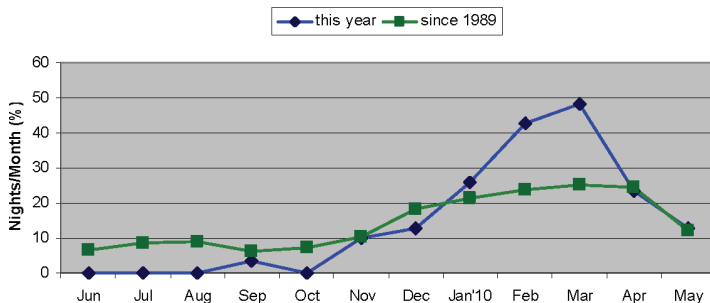


Figure 1. — Nightly 225-GHz opacity Mauna Kea <0.05.

Nightly 225-GHz Opacity Mauna Kea < 0.08

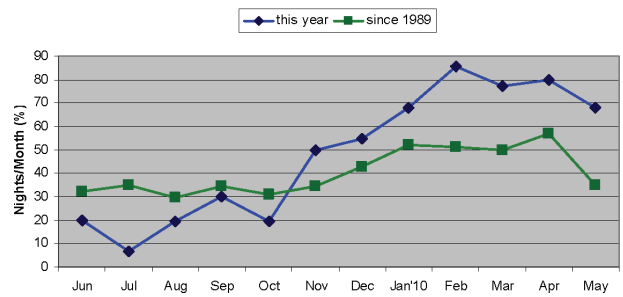


Figure 2. — Nightly 225-GHz opacity Mauna Kea <0.08.

(Director's Desk, continued from page 3)

fault rate for the observatory over the six-month period between October 2009 and March 2010 below the 5% mark (a target set by the JCMT Board). We now regularly see weeks where the fault rate falls below 3% of clear time lost in that week. This is an excellent step forward in our operations. Congratulations to our engineering, software and JCMT staff in achieving this.

HARP underwent a minor but risky "surgical operation" in February when the 3 receptors that failed in November 2009 were replaced by spares. This work went smoothly and the instrument has since performed very well with 15 receptors. The last receptor that remains unusable has a fault which we believe is associated with the cryogenic wiring. This requires the focal plane to be disassembled which is an inherently risky operation. At present we will not considering taking such a risk until we have to open up the instrument for some other reason.

Finally, we have a large number of

staffing changes to report on this occasion. Walther Zwart left us in November to return to the Netherlands, having spent three years at the JAC as a software engineer developing the ACSIS control and data reduction code. His excellent work left us with an easily-supported system, which is in part responsible for the low fault rate in recent months. John Pascual, electronics technician, also left in November to move to a position at the SMA. James Webb (no relation to JWST!) joined us in that same month as an electronics engineer, having recently obtained his doctorate in quantum optics at the University of New South Wales. Stuart Putland, Head of Administration, completed his tour of duty in December and returned to the Ministry of Defence in the UK, from whence he was seconded; the position was re-named to Head of Corporate Services and the new holder of this position is Linda Fisher, formerly Head of Human Resources and Estates Management at the UK ATC. Also in December, Ming Zhu left the JAC at the expiry of his contract with the National Research Council of Can-

ada; Ming will be replaced by Chris Davis, who will transfer over from the UKIRT science group as part of the aforementioned operational changes at UKIRT. Besides being a good move for Chris, this is an excellent appointment for the JCMT since Chris is a productive senior astronomer with a background in submillimetre astronomy.

Moving into 2010, Brad Cavanagh, software engineer in the Scientific Computing Group, left us in January to move to the University of British Columbia. A recruitment process to replace Brad is underway. Michele Mulkey, HR Manager, left the JAC in March. Finally, TSS Ben Warrington left us in May after several years to move to a position in Australia, where his wife has commenced a PhD programme, and we have recruited former TSS Jeff Cox as a temporary part-time replacement, pending a recruitment later in the year. ●

# Comparisons of Cold Dust, Polycyclic Aromatic Hydrocarbons, Molecular Gas, and Atomic Gas in NGC 2403

George Bendo (*Imperial College London*) & The JLS NGS Consortium

The JCMT Legacy Survey (JLS) Nearby Galaxies Survey (NGS) is an 850  $\mu\text{m}$  and CO J=(3-2) survey with the goals of studying molecular gas and dust in a representative sample of galaxies within 25 Mpc. These data when combined with existing 3.6-160  $\mu\text{m}$  data from the Spitzer Infrared Nearby Galaxies Survey (Kennicutt et al. 2003) and HI data from The HI Nearby Galaxies Survey (Walter et al. 2007) provide a powerful dataset for

studying the properties of the interstellar medium (ISM) on sub-kiloparsec scales within nearby galaxies. We used CO J=(3-2) from the NGS along with these other surveys to study the spiral galaxy NGC 2403. This is a  $21.9 \times 12.3$  arcmin<sup>2</sup> SABcd galaxy (de Vaucouleurs et al. 1991) at a distance of  $3.13 \pm 0.14$  Mpc (Freedman et al. 2001); HARP can resolve structures  $\sim 200$  pc in size in this galaxy. We had two goals in

this work. The first was to understand spatial variations in the gas-to-dust ratios on sub-kpc scales. The second was to further examine the relation between the radial profiles of polycyclic aromatic hydrocarbon (PAH) emission and CO emission reported by Regan et al. (2006). The detailed results are presented by Bendo et al. (2010) in the third paper from the JCMT NGS; we present

(JLS NGS, continued on page 6)

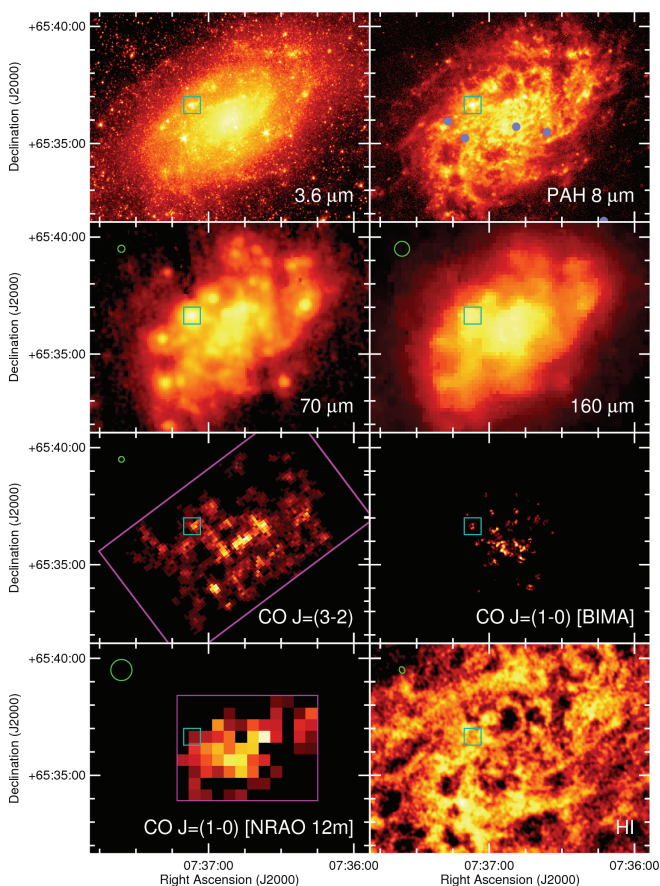


Figure 1. — Images of the inner  $12 \times 9$  arcmin<sup>2</sup> of NGC 2403 in multiple wave bands. Logarithmic colour scales are used for all images except the 160  $\mu\text{m}$  image, where the logarithmic scale to the second power was used to enhance the structure in the image, and the CO images, where a linear colour scale was used. The green circles show the full-width at half-maximum (FWHM) of the point spread function (PSF) except in cases where it was smaller than 5 arcsec. The cyan box shows VS 44 (the brightest source in the mid-infrared). The magenta boxes show the observed regions in two of the CO images; note that regions with no detections were made black.

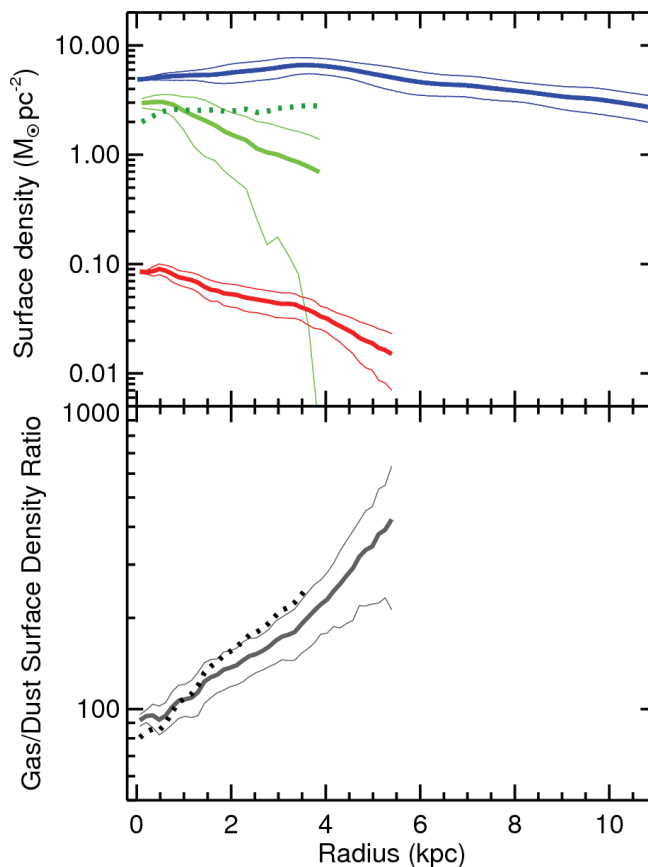


Figure 2. — Radial profiles of the HI surface density (solid blue line, top panel), H surface density (green lines, top panel), and dust surface density (solid red line, top panel) as well as the total (molecular and atomic) gas-to-dust surface density ratio (bottom panel). These radial profiles were measured in data where the PSFs were matched to the PSF of the 160  $\mu\text{m}$  data, which has the largest FWHM (38 arcsec). For the H and gas/dust ratios, the solid lines are for quantities calculated using a constant  $X_{\text{CO}}$  and the dotted lines are for quantities calculated using a value of  $X_{\text{CO}}$  that depends on  $12 + \log(\text{O}/\text{H})$ . The standard deviations of the data are plotted as thinner lines around the radial profiles (except for quantities based on the variable  $X_{\text{CO}}$  which have standard deviations similar to corresponding quantities with a constant  $X_{\text{CO}}$ ). Radial profiles are truncated at their detection limits. The gas-to-dust ratio calculated using the variable  $X_{\text{CO}}$  is truncated at 4 kpc to show how the change in  $X_{\text{CO}}$  affects this ratio; beyond this radius, the radial profile merges back into the other gas-to-dust radial profile.



(JLS NGS, continued from page 5)

here a brief summary of the main results.

Figure 1 shows the central  $12 \times 9$  arcmin<sup>2</sup> of NGC 2403 as observed in multiple wave bands. The  $3.6 \mu\text{m}$  image traces starlight. The  $8.0 \mu\text{m}$  image primarily traces PAH emission. The 70 and  $160 \mu\text{m}$  images trace  $\sim 20$  K dust that constitutes the bulk of the dust mass in the galaxy. The CO emission traces molecular gas, while the HI emission traces atomic gas. Note that many regions that appear bright in the CO emission also have counterparts in the 8- $160 \mu\text{m}$  bands. The region VS 44, which is marked with a cyan square, is particularly noteworthy; this is the brightest source at mid-infrared wavelengths. Also note that the HARP data detected emission from a much larger area than the BIMA data from Helfer et al. (2003) and have a smaller PSF than the NRAO 12 m data from Thornley & Wilson (1995).

We used the NRAO 12 m data with

the HARP data to determine the CO  $J=(3-2)/J=(1-0)$  line ratio. Globally, this value is 0.69, but the values range from 0.11 to 1.2. We also found a function that describes the ratio as a function of CO  $J=(3-2)$  intensity and galactocentric radius. Using this function and  $X_{\text{CO}}$  values derived for CO  $J=(1-0)$ , we could calculate molecular gas surface densities that could be used to study the gas-to-dust ratio.

Figure 2 shows the radial profiles of the dust surface density (calculated from the 70 and  $160 \mu\text{m}$  data), the atomic gas surface density, and two variants of the molecular gas surface density. Below this, we show the gas-to-dust ratio, which varies from  $\sim 100$  near the nucleus to  $\sim 400$  at 5.5 kpc, which is the limit at which we can measure the dust surface density. We also show a map of the gas-to-dust ratio in Figure 3. Except for the radial variations in the ratio, the map looks relatively featureless; even VS 44 disappears in the map. This demonstrates that the gas-to-

dust ratio primarily depends on radius, which implies that variations in the ratio are related to metallicity. The gradient in  $12+\log(\text{O}/\text{H})$  based on several references (see Bendo et al. 2010) is  $-0.084 \pm 0.009$  dex/kpc. For comparison, the gradient in the dust-to-gas ratio, expressed as  $d[\log(\sigma_{\text{dust}}/\sigma_{\text{gas}})]/dr$ , is  $-0.097 \pm 0.002$  dex/kpc. The close correspondence between these gradients provides further evidence that the gas-to-dust ratio varies as a function of metallicity.

Figure 4 shows the radial profiles of the HI intensity, the CO  $J=(3-2)$  intensity, and the stellar-continuum subtracted  $8 \mu\text{m}$  surface brightness (which we will refer to as PAH  $8 \mu\text{m}$  emission for simplicity). As can be seen from this figure, the radial profile of the HI emission is roughly flat, while the CO  $J=(3-2)$  and PAH  $8 \mu\text{m}$  radial profiles are roughly parallel. The CO  $J=(3-2)$  radial profile has a scale length of  $2.0 \pm 0.2$  kpc between 0.5 and 4 kpc, while the PAH  $8 \mu\text{m}$

(JLS NGS, continued on page 7)

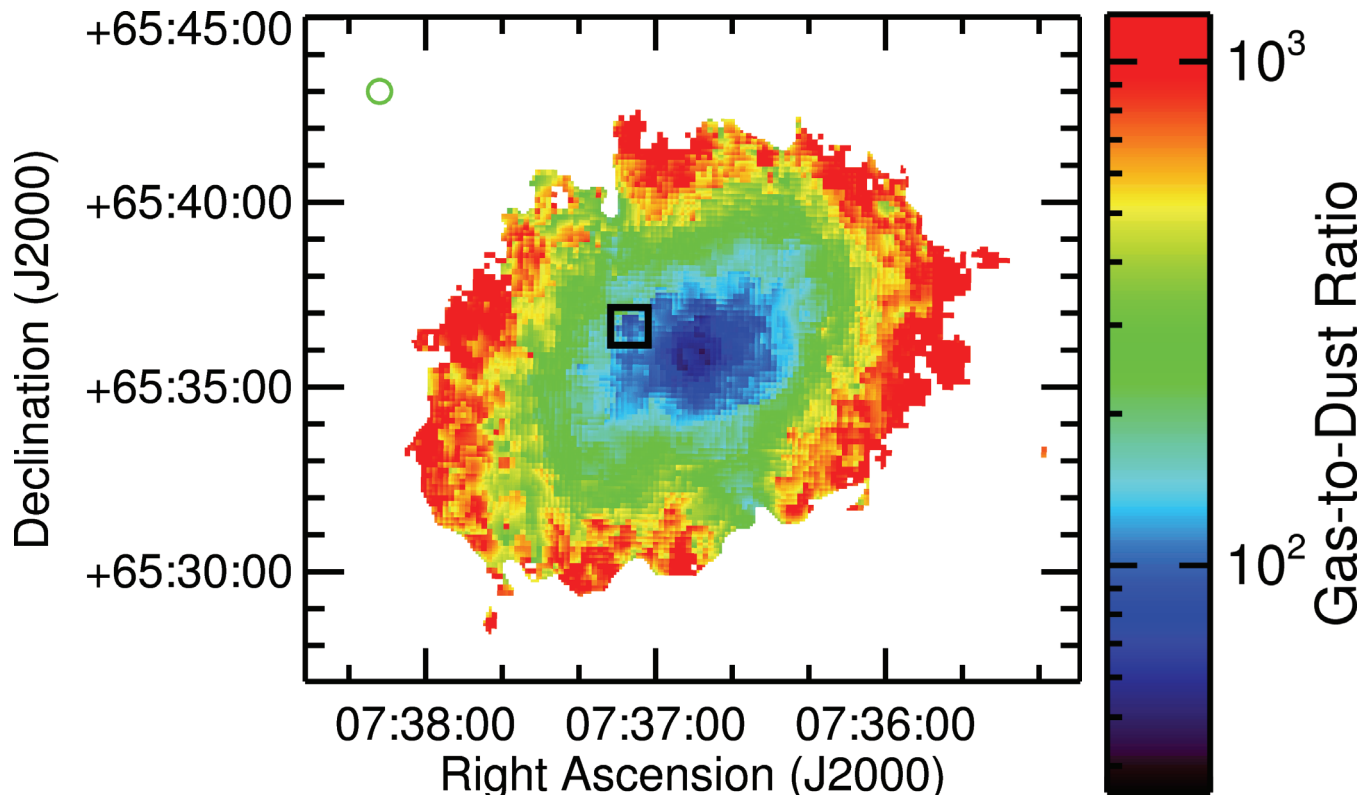


Figure 3. — Image of the gas-to-dust surface density ratio in NGC 2403. The image is  $21 \times 18$  arcmin<sup>2</sup>. Only pixels where the dust mass was measured are shown. The molecular gas surface densities were calculated assuming that  $X_{\text{CO}}$  is constant, although the functionality of  $X_{\text{CO}}$  does not strongly affect the appearance of this figure. The green circle in the upper left corner shows the 38 arcsec FWHM of the PSF, which is equivalent to the PSF of the  $160 \mu\text{m}$  data. The black square indicates the location of VS 44.

(JLS NGS, continued from page 6)

radial profile measured within the same range (and within data where the point spread function was matched to that of the HARP data) has a scale length of  $1.99 \pm 0.04$  kpc. This result closely resembles the correspondence between the radial profiles of PAH  $8 \mu\text{m}$  emission and CO  $J=(1-0)$  emission found by Regan et al. (2006). However, the dispersion in the ratio of the radial profiles is very high, and a point-by-point comparison in the maps shows a poor quantitative correspondence between the CO  $J=(3-2)$  intensity and the PAH  $8 \mu\text{m}$  surface brightness. This dispersion on sub-kiloparsec scales is the main reason why the ratio of the radial profiles dips within the inner 0.5 kpc.

The radial profiles for CO  $J=(3-2)$  and PAH  $8 \mu\text{m}$  emission could be linked through a couple of mechanisms that would not require a one-to-one correspondence on sub-kpc scales. First of all, the PAH and CO emission could be linked by the stellar potential wells that have been hypothesized as the regions where molecular clouds are formed (e.g. Leroy et al. 2008). The molecular clouds would produce CO emission, while the increase in the radiation field in these potential wells would enhance PAH emission in nearby locations not necessarily in the potential wells themselves. Alternatively, both PAH and CO emission could be affected by similar excitation mechanisms connected to star formation. Knapen & Beckman (1996) suggested that cosmic rays from star forming regions could excite the CO emission. Meanwhile, PAHs would be heated by the optical and ultraviolet light from star forming regions, although the PAHs may be destroyed within the regions themselves. However, it is just possible that this correspondence between CO and PAH emission in NGC 2403 is just a coincidence. As work continues with the JCMT NGS, we will be examining this relation between PAH and CO emission for a larger number of spiral galaxies to understand whether this relation applies to other galaxies as well.

References

Bendo, G. J., et al., 2010, MNRAS, 402, 1409.  
 de Vaucouleurs G., et al., 1991, Third Reference Catalogue of Bright Galaxies, Springer-Verlag, Berlin.  
 Freedman W. L. et al., 2001, ApJ, 553, 47.  
 Helfer T. T., et al., 2003, ApJS, 145, 259.  
 Kennicutt, R. C., Jr., et al., 2003, PASP, 115, 928.  
 Knapen J. H., Beckman J. E., 1996, MNRAS, 283, 251.  
 Leroy A. K., et al., 2008, AJ, 136, 2782.  
 Regan M. W. et al. 2006, ApJ, 652, 1112.  
 Thornley M. D., Wilson C. D., 1995, ApJ, 447, 616.  
 Walter, F., et al., 2008, AJ, 136, 2563. ●

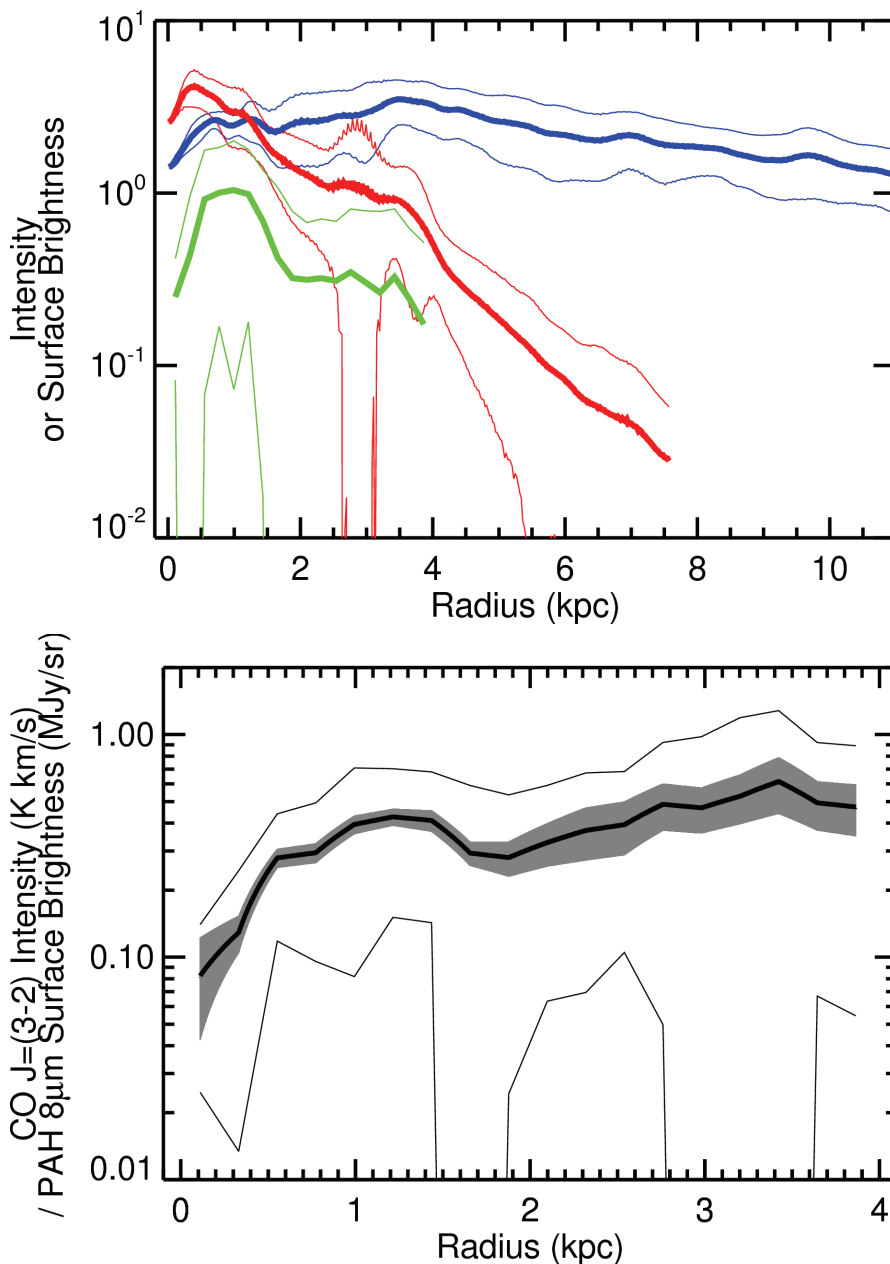


Figure 4. — Radial profiles of the HI intensity in Jy/beam km/s (top panel, blue line), CO  $J=(3-2)$  intensity in K km/s (green line, top panel), and PAH  $8 \mu\text{m}$  surface brightness in MJy/sr (top panel, red line) as well as the ratio of CO  $J=(3-2)$  intensity to PAH  $8 \mu\text{m}$  surface brightness (black line, bottom panel). Then radial profiles were measured in data where the PSFs were matched to the PSF of the CO  $J=(3-2)$  data, which has a FWHM of 14.5 arcsec. The standard deviations of the data are plotted as thinner lines around all radial profiles. The uncertainties in the mean values are generally smaller than the thicknesses of these lines except in the case of the CO  $J=(3-2)$ /PAH  $8 \mu\text{m}$  emission ratio, where the uncertainty is shown as a shaded grey region.



## Probable Collision between a Comet and Saturn Two Centuries Ago

Thibault Cavalié (*MPI Lindau*), Françoise Billebaud, Michel Dobrijevic (*Bordeaux*), Paul Hartogh (*MPI Lindau*), Thierry Fouchet, Emmanuel Lellouch, Thérèse Encrenaz (*Observatoire de Paris*), Jean Brillet (*Bordeaux*), Gerald Schieven (*HIA/NRC*), & Jan Wouterloot (*JAC*)

Between July 16th and July 22nd, 1994, more than 20 fragments of comet P/Shoemaker-Levy 9 (SL9) hit Jupiter. These impacts generated explosions in the atmosphere of the planet that remained observable for several weeks in the form of dark spots on the Jovian disk. It was the first time ever that such a collision has been observed in the Solar System. Observations of CO in Saturn performed at the JCMT in 2008 and 2009 indicate that such an impact possibly occurred two centuries ago in the atmosphere of this planet.

CO was detected in the atmosphere of Saturn at  $4.7 \mu\text{m}$  back in 1986 by Noll et al. (1986) but its origin remained controversial (Noll and Larson, 1991). Actually, the question of the origin of CO in giant planet atmospheres is part of a wider issue: the origin of oxygen in giant planet atmospheres.  $\text{H}_2\text{O}$  and  $\text{CO}_2$  have been detected in the stratospheres (upper part of atmosphere) of the giant planets with ISO and Spitzer (Feuchtgruber et al. 1997; Burgdorf et al. 2006). The presence of these

condensable species above the tropospheric cold trap of these atmospheres implies an external origin. Several kinds of sources have been postulated: local (icy rings and satellites), diffuse (interplanetary dust particles) and sporadic sources (SL9-like comet impacts). In contrast, observing CO in the stratosphere of a giant planet does not imply an external origin. Indeed, this species does not condense at the tropopause. Thus, an additional source is likely to provide CO to the stratospheres of the giant planets, in the form of upwards convective mixing originating from the deep hot atmosphere.

We have conducted observations of CO in Saturn at JCMT in order to determine its origin. Observations were performed in January 2008 and in January-March 2009. We first used HARP to measure the CO(3-2) line. This line, probing the 1-10 mbar levels (or even deeper), could cover several GHz as in Neptune (see Hesman et al. 2007) due to pressure-broadening. This is why we

used the Hesman et al. (2007) technique of observing Saturn with several continuous 1 GHz bands with 50% overlap in order to cover 5 GHz. This resulted in the first detection of CO in Saturn in the submillimeter (see Figure 1, left). One year later, we observed the CO(6-5) line with the RxWD receiver over a 250 MHz band to focus only on the stratospheric emission peak of the line, formed at the 0.1-1 mbar levels. To achieve baseline stability, we adopted a "limb-switching" technique, that takes advantage of the relatively small beam ( $\sim 7$  arcsec) compared to the planet size ( $\sim 19$  arcsec). It consists of (i) observing alternately the eastern and western limbs (both sharing a common OFF position), and (ii) subtracting one spectrum from the other (see Figure 2). The lines, Doppler-shifted by the rapid rotation of the planet ( $\sim 9.5$  km/s at the equator), are still present in the final spectrum, one with a positive amplitude and one with a negative amplitude (see Figure 1, right).

(Saturn, continued on page 9)

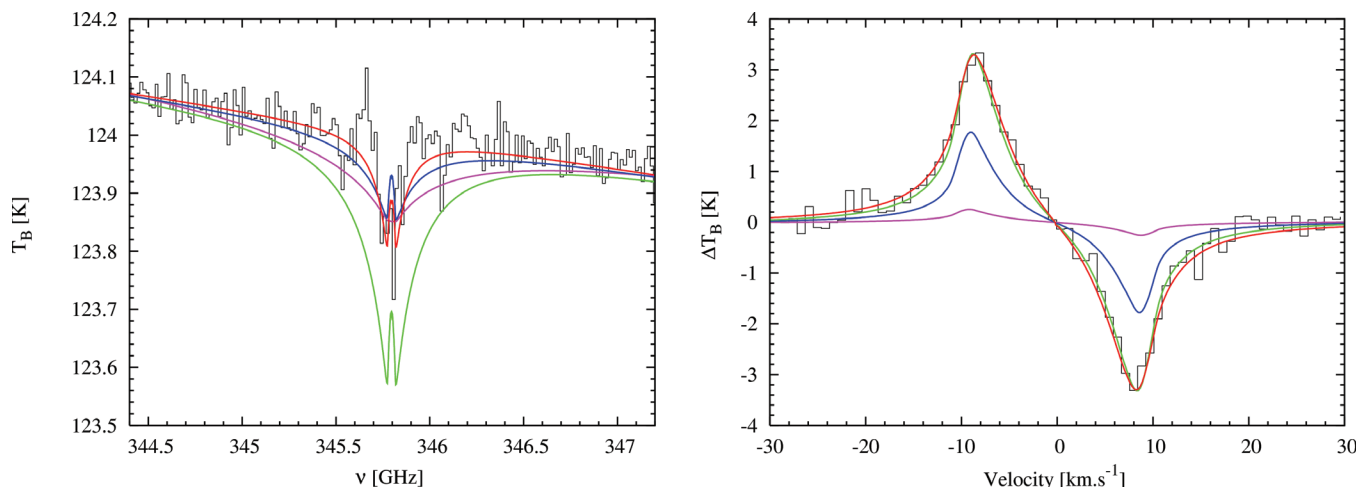


Figure 1. — CO(3-2) (left panel) and CO(6-5) (right panel) spectra of Saturn obtained with JCMT in January 2008 and in January-March 2009 (respectively). Synthetic spectra were computed from the vertical profile generated by our 1-D transport model. The pink line corresponds to a purely internal source of CO, the blue and green lines correspond to an external steady source (local or diffuse) of CO and the red line corresponds to the impact of an SL9-like comet 220 years ago. Only the latter model reproduces both observations consistently.

(Saturn, continued from page 8)

To determine the origin of CO in Saturn, we developed a 1-D model of the vertical transport of CO in Saturn's atmosphere in order to generate vertical profiles of CO as a function of the source(s) of CO. We then used a 1-D line-by-line radiative transfer model that accounts for the ellipsoidal geometry of the planet and for the limb emission to obtain the translation of the calculated vertical profiles in terms of spectra.

Our first conclusion while analyzing the CO(3-2) spectrum was that CO had an external source. As seen on Figure 1 (left, pink line), a purely internal source results in too wide

an absorption feature. This result would later be confirmed by our CO (6-5) observation (see Figure 1, right, pink line). So, we were unable to measure any internal component in the CO abundance profile. However, a weak component could have been filtered out while removing the baseline ripple from the CO(3-2) spectrum. From this spectrum, we could determine an upper limit on the internal CO mixing ratio:  $1 \times 10^{-9}$ . Since the tropospheric mixing ratio of CO is proportional to the deep  $H_2O$  abundance, we used this value to constrain the deep O/H ratio in Saturn. This parameter is of prime importance to understand the physico-chemical processes that led to

the condensation of Saturn's core. We found that the Saturn's deep O/H ratio is lower than 26, implying that the more likely process that led to the formation of its core was condensation in amorphous ices. However, the clathration process hypothesis cannot be totally ruled out.

The CO(3-2) observation, though showing an external source of CO, did not enable us to discriminate between a steady source (local or diffuse) and a sporadic source. This is the reason why we observed Saturn again, but at a higher frequency. Our CO(6-5) limb-switched observations allowed us to measure the abundance of CO at a lower pressure level than the CO(3-2) ones. Thus, we were able to put a second constraint on the vertical profile of CO. Using our transport model again, we analyzed jointly both CO spectra. The conclusion of our modeling is that the most probable source for CO was the impact of a comet  $\sim 3 \times$  more massive than SL9 220 years ago. According to Zahnle et al. (2003), such an impact occurs every 750 years in Saturn. Indeed, the comet modeling parameters were consistent for observations from both CO transitions (red line in Figure 1), whereas there was no single value of steady flux that could do the same (green and blue lines in Figure 1).

When considering this result in the frame of recent observations of CO in giant planets (Bezard et al. 2002 for Jupiter, Lellouch et al. 2005 and Hesman et al. 2007 for Neptune), we see that SL9-like comet impacts could be the main suppliers of CO to giant planet stratospheres.

For further details, please refer to Cavalié et al. (2008) and Cavalié et al. (2009).

References

Bézard et al. 2002. Icarus 159, 95-111.  
 Burgdorf et al. 2006. Icarus 184, 634-637.  
 Cavalié et al. 2008. Icarus 203, 531-540.  
 Cavalié et al. 2009. A&A 510, A88.  
 Feuchtgruber et al. 1997. Nature 389, 159-162.  
 Hesman et al. 2007. Icarus 186, 342-353.  
 Lellouch et al. 2005. A&A 530, L37-L40.  
 Noll et al. 1986. ApJ 309, L91-L94.  
 Noll and Larson 1991. Icarus 89, 168-189.  
 Zahnle et al. 2003. Icarus 163, 263-289. ●

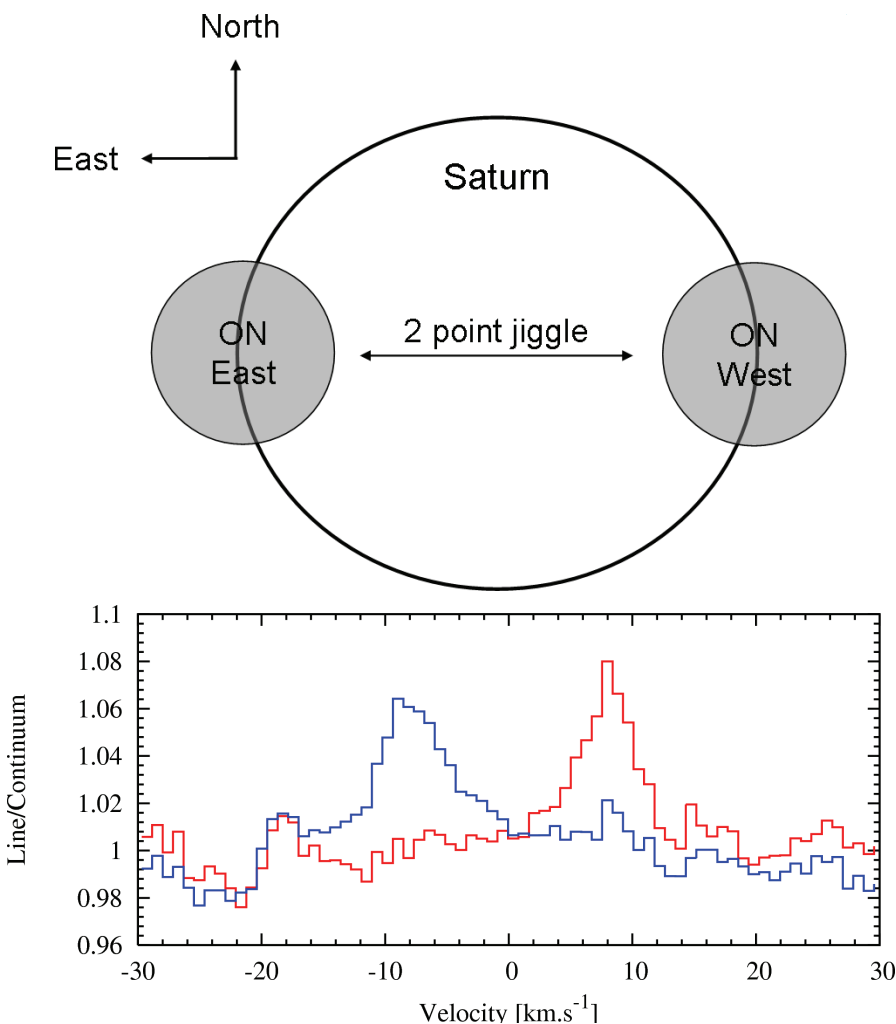


Figure 2. — (top panel) On-scale scheme representing the limb-switching technique adopted for the CO(6-5) observations. The larger disk represents Saturn while the smaller ones represent the JCMT beam. The center of the beam is alternately pointing towards the eastern and the western limbs before observing a common OFF position 60 arcsec away from Saturn. (bottom panel) Raw spectra of the eastern (blue line) and western (red line) limbs of Saturn at the CO(6-5) frequency in Saturn's reference frame. The CO line is detected in each spectrum and effect of the rotation of Saturn is clearly seen. This plot also shows baseline features that are canceled out by subtracting the western spectrum from the eastern one.





## Automated Feature Extraction with HARP Data

Chris Beaumont Jonathan Williams (*Hawaii*)

Anyone who has used HARP to map star forming regions knows the spectacular kinematic and spatial detail that the instrument delivers. He or she also appreciates how challenging it can be to analyze these data. The mosaics that HARP creates show intricate structures of gas shaped by turbulence, gravity, and stellar feedback. The sensible first analysis step — identifying and cataloging these features — is complicated by the fact that emission from different structures in a star forming region often overlaps in a spectral data cube. This early hurdle complicates all subsequent analysis of the data.

The human eye is actually quite good at deblending cloud emission, when the overlapping structures have different morphologies (examples include protostellar outflows, pillars, and wind-blown cavities embedded in larger clouds). However, the process is difficult to automate using standard techniques like intensity thresholding, edge detection, fourier filtering, etc. Consequently, structures are manually cataloged — a time consuming, subjective, and error-prone approach.

We have been exploring new ways to robustly and automatically deblend structures in molecular cloud data. On a recent HARP imaging campaign of CO in the M 17 cloud, we serendipitously observed a large (20 arcmin) background supernova remnant (SNR). These two objects are ideal for exploring source-extraction techniques; while emission from M 17 and the background remnant overlap, their morphologies are strikingly different. M 17 is spatially extended and diffuse, with typical line widths of  $\sim 1-3$  km/s (FWHM). The supernova remnant, by contrast, is filamentary and — due to the strongly shocked gas — has line widths exceeding 20 km/s.

We have found that machine learn-

ing algorithms are effective at discriminating between these two structures. These algorithms use training data to infer patterns in different classes of objects. In our application, the training set consists of several pixels identified, by eye, as belonging to M 17 and the SNR. For each training example, we extract a “feature vector” — a list of intensities of the neighboring pixels. These feature vectors are then used to identify the distinguishing characteristics of the cloud and SNR.

The specific technique underlying our approach is the Support Vector Machine (SVM) algorithm (Joachims 1999). The algorithm interprets feature vectors as coordinates for points in a high-dimensional space. Using the training data, it derives a boundary surface to partition the points from each structure. Unclassified feature vectors are then labeled according to the side of the boundary on which they fall. Very general decision surfaces can be derived in this way, and thus SVMs can infer sophisticated patterns in the training set, even without domain-specific knowledge of what the data describe. For example, SVMs are used by the US Post Office to read and sort hand-written addresses on envelopes (Desealers et al. 2010).

We are encouraged by how the SVM algorithm performs when classifying structures in star forming regions. Figure 1 shows a fully automated segregation of our M 17/SNR data. Each image is a slice through the original data cube. Emission identified as belonging to the supernova is colored blue, while cloud emission is colored red. Despite the large morphology differences between these slices, the algorithm correctly identifies most pixels. An animation of the full cube classification is available at <http://www.ifa.hawaii.edu/~beaumont/deblend.html>.

We are currently working to further optimize the algorithm’s performance; at the moment, most misclassifications occur along the edges of structures (in position-position-velocity space), and at very faint pixels. Our longer-term goal is to extend the method to extract objects of interest — pillars, shells, outflows — within a single star forming region. These structures are both more blended and less morphologically distinct than the two objects in our current dataset. However, we are impressed by the SVM algorithm’s ability to recognize complex morphologies in our data, and optimistic that the approach will generalize well to other regions. Our hope is that this method will provide researchers with a new tool to more fully exploit the exquisite datasets that the JCMT provides.

### References

- Joachims, T. Making large-Scale SVM Learning Practical. *Advances in Kernel Methods - Support Vector Learning*, B. Schölkopf and C. Burges and A. Smola (ed.), MIT-Press, 1999.
- Desealers T., Heigold, G., Ney, H. *Pattern Recognition*. Vol. 43. Issue 7. July 2010. pp. 2476-2484. ●

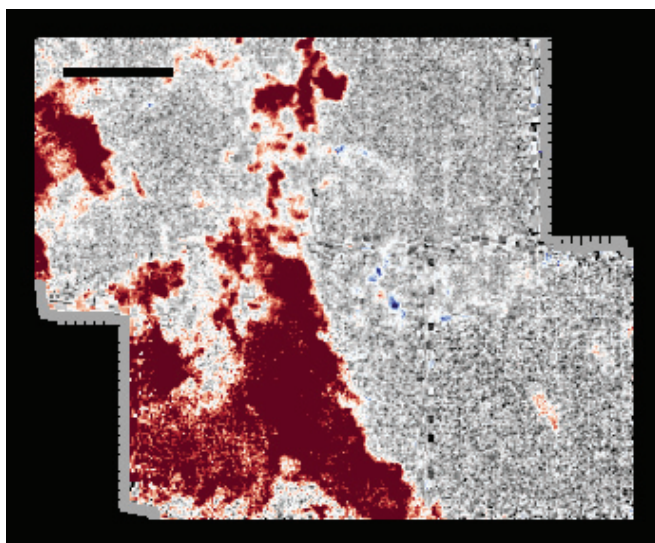
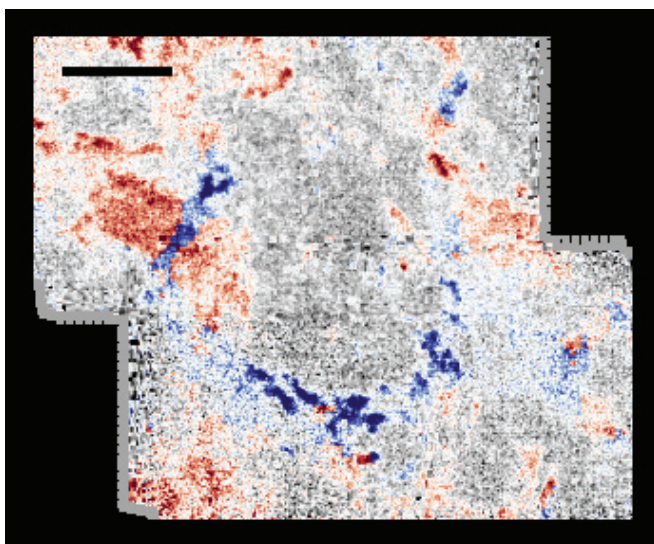
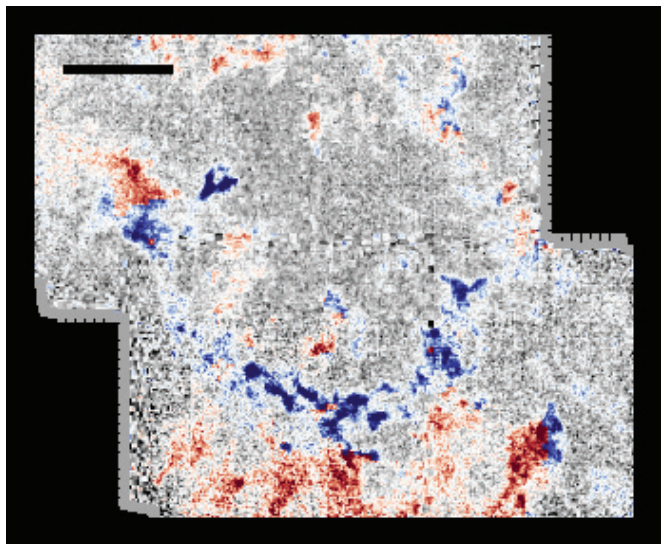


Figure 1. — An automated classification of cloud emission. Shown are three constant-velocity slices through a CO 3-2 data cube. Emission classified as belonging to the SNR is colored blue, while cloud emission is colored red. The scale bar is 6 arcmin long (5 pc at 3 kpc, the estimated distance of the SNR).





# The SCUBA-2 Shared-Risks Observing Campaign: An Overview

Antonio Chrysostomou (*Associate Director JCMT*)

## *Introduction*

At its meeting in June 2009, the JCMT Board decided that following a period of on-sky commissioning with SCUBA-2 (initially with just 2 sub-arrays in its focal plane) there should be a brief campaign of shared-risks observing. This would serve to get the JCMT community involved with the instrument but, importantly, to also obtain some early science results from SCUBA-2 to demonstrate the instrument's potential.

To this end, a sub-committee of Board members was formed to formulate a set of recommendations under which to run the SCUBA-2 Shared Risks Observing (S2SRO) campaign. Time which had originally been put aside for SCUBA-2 commissioning, as well as other E&C projects, was put towards S2SRO. Overall, 276 hours were made available for an S2SRO campaign and, after just a month of instrument technical commissioning, a call for proposals was issued at the end of October 2009.

## *S2SRO Proposals*

In order to maximize the output from the S2SRO campaign, the call for S2SRO proposals stipulated that no single proposal should ask for more than 10 hours of observing time. In all, there were 59 proposals received asking for a total of 447 hours. With the University of Hawaii claiming their share of 31 hours, this gave a direct oversubscription of almost a factor of two. Taking into account the number of hours requested per weather band this oversubscription comes closer to 3 or 4 (*e.g.*, bands 1 and 2 were heavily oversubscribed whereas band 4 was not). An excellent result given that proposals were restricted to be no longer than 10 hours and a good sign of community interest in SCUBA-2.

The ITAC met in November to consider these proposals. This was a special meeting of the ITAC, and for the purposes of S2SRO only its membership was expanded to include Peter Barthel and Tracy Webb. Of the 59 proposals received, the ITAC allocated time to 40 proposals, purposefully overloading the bands 1-3 weather queues. The allocated projects had an even spread of subject themes, with 21 extragalactic and 19 Galactic projects. Recognising the fact that just one array per waveband was in the instrument (and the 10-hour limitation) 19 proposals requested data on the order of, or smaller, than the field of view of the instrument (approximately 3 arcminutes), with a further 16 proposals requesting time to map fields less than 1 degree in scale.

## *S2SRO Campaign*

At the time that the S2SRO call was made, the intention was to start the campaign in December so that first science results would be available by Christmas. Unfortunately, as the project entered its truncated phase of on-sky commissioning in November, it was clear that this would not be so. There were concerns with the frequency of instrument warm-ups and the noise performance of the arrays, and the quality of the resultant maps was proving to be not as anticipated at the time that the call was made.

New observing modes were devised in an effort to alleviate the issue of low-frequency noise on maps. In particular, the "rotating pong" observing mode for large fields proved to be useful for minimising its impact, although it did not eliminate it.

Following an internal review, S2SRO was given the go ahead in January 2010 and the campaign started in mid-February. Six weeks into the instrument cooldown the fridge was performing well, showing no signs

of imminent warm-up that had been seen in the past. Given this, S2SRO was extended further into March. Unfortunately, a power fault caused SCUBA-2 (and other facility instruments) to warm up and although all attempts were made to recover, it was not possible to get SCUBA-2 back to a stable base temperature — a blockage in the dilution refrigerator had developed following the uncontrolled warm up. Given that the instrument was scheduled to be warmed up the following week anyway, to extract the arrays so they could be shipped back to the UK ATC for upgrading to new cold electronics modules, it was decided to end the S2SRO campaign at that point.

Overall, and including projects observed by the University of Hawaii, there were a total of 28 projects observed. Of these, 19 obtained 100% of their allocated time, or more, with seven getting between 50% and 100% of their request. Eight hours were observed for the SCUBA-2 project team as part of their guaranteed time.

## *Post-S2SRO and What Happens Next*

Since the end of S2SRO, the primary focus of the SCUBA-2 project team has been for the data reduction software to produce the best maps possible, calibrated to useful limits of 20% or better. Given the performance of the arrays and instrument, this has been a detailed and time consuming process. Many improvements to the software have been made and many of the S2SRO PIs have been involved with the SCUBA-2 team in providing feedback. It is not an underestimate to say that this feedback has been very valuable to the project team and it is much appreciated.

The aim of the S2SRO campaign was to produce some early SCUBA-2 sci-

*(S2SRO, continued on page 13)*

## Observing Using Frequency Switching

Per Friberg (*JCMT Head of Instrumentation*)

### Introduction

Frequency switching has been commissioned with RxA and HARP using ACSIS as a backend. The method is best suited for weak narrow lines but can also be used when it is hard to find an off position. Frequency switching works best for HARP but is usable with RxA with some extra care. The OT supports setting up frequency switched observations.

### The Method

Normally spectra are formed by subtracting an off spectrum from an on spectrum and dividing by the off spectrum. When observing using frequency switching the reference spectrum is not obtained at an offset position. It is obtained by shifting the first LO frequency a small amount. Typically the LO is shifted between 8-32 MHz. Thus the line is observed in both the on and off spectra. The result is a spectrum with one line being negative and another positive. After post-processing this gives an improved S/N for the same observing time compared to position switching. However, the shifting in frequency also creates a number of problems. Interference spikes will be doubled. Atmospheric CO and ozone lines that normally are cancelled can appear in the spectra. Further, the small shift in the first LO causes changes in impedance and can create standing waves in the SIS mixer. Depending on the design this can cause baselines. With modern tunerless mixers the baselines are generally well behaved or absent. The limited amount we can switch the first LO combined with the baseline issues are the reasons frequency switching is normally used for narrow lines.

### Noise Estimates

The noise level in the on or off total power spectrum is computed according to the standard formula:

$$dT_{rms} = \alpha \frac{T_{sys}}{\sqrt{df \cdot \tau}}$$

Here  $\alpha$  is a factor taking into account the small degradation inherent in ACSIS,  $\tau$  is the integration time excluding overheads and  $df$  the channel spacing in ACSIS. When we form the spectrum by subtracting two spectra the square of the noise is added. In addition we only spend half of the time in each of the on and off spectra. Thus we end up with:

*(Frequency Switching, continued on page 14)*

*(S2SRO, continued from page 12)*

ence results with community involvement. Many of you reading this may have already seen some of the early results that have been presented at various national and international meetings that attest to this. Nevertheless, it is disappointing that the sensitivity of the instrument was not as we had anticipated at the time the call for proposals was issued. In the main, the reduced sensitivity is dominated by: a thermal path between the 1-K box and the arrays resulting in a power gradient across the arrays which restricts the pixel yield and creates a spread in pixel sensitivity, low frequency thermal

fluctuations from the refrigerator, and relatively low scanning speeds (especially for small fields). Upgrades to the instrument are in place that are expected to account for the first two of these, and new observing modes will be commissioned in the next phase of the project, with the full set of eight arrays, to tackle the last of these.

At the time of writing the data reduction software and associated documentation is being finalised, ready for release to S2SRO PIs and their teams. This will culminate in the first science papers exclusively using SCUBA-2 data appearing be-

fore the end of the year, and in the next edition of this Newsletter.

In the meantime, the SCUBA-2 project is preparing to enter its next phase. In the next weeks the instrument will be upgraded to its full complement of arrays, four at each of the 450  $\mu\text{m}$  and 850  $\mu\text{m}$  bands. Following this a period of array commissioning will begin to fully understand and characterise the performance of each of these arrays before we begin the final phase of on-sky commissioning. We will keep the community informed of the milestones as they are reached. ●



(Frequency Switching, continued from page 13)

$$(dT_{rms})^2 = \frac{(\alpha T_{sys})^2}{df \cdot \tau_{total} / 2} + \frac{(\alpha T_{sys})^2}{df \cdot \tau_{total} / 2} \Rightarrow dT_{rms} = 2\alpha \frac{T_{sys}}{\sqrt{df \cdot \tau_{total}}}$$

This formula is valid for a position switch observation and the raw frequency switched spectrum. We then post-process the frequency switched observation by taking a copy of the spectrum, invert it, shift by the frequency switch amount, add it to the original and divide by two. The addition again increases the noise by adding it squared but the division reduces the squared noise by a factor of four and we have:

$$dT_{rms} = \sqrt{2}\alpha \frac{T_{sys}}{\sqrt{df \cdot \tau_{total}}}$$

The time needed to reach the same noise level is halved compared to standard position switch. We should also compare this to on-the-fly raster mapping. In a raster the noise for each of the  $n$  spectra in a raster row is:

$$dT_{rms} = \frac{T_{sys}}{\sqrt{df \cdot (\tau_{total} / n)}} \left(1 + \frac{1}{\sqrt{n}}\right)$$

If we compare this with the time it would take to obtain  $n$  frequency switched spectra we find that raster mapping is superior for  $n$  equal to or larger than 6. Overheads will increase this number slightly. However, for a larger area raster mapping is superior. This is why frequency switching is mainly used for weak lines in limited positions. If the lines were strong we would likely map a larger area using raster scanning. A combined frequency switch raster mode would have inferior noise performance to a raster map.

### Limitations with RxA

The current RxA has a very old computer from the late 1980s using a z80 micro processor with a clock rate of 4 MHz. Further, it is not designed for the synchronization scheme that the antenna, HARP, and ACSIS are using. As a result the first spectrum in each observation are not acquired correctly — the frequency switch distance is only half the expected amount. RxA is much slower in starting up than HARP & ACSIS and it has no way to delay the start of observing until it is ready. The latter problem also applies to the locking problem during observations — it is important to monitor the RxA engineering screen for locking problems during frequency switched observations. For these reasons it is strongly recommended that test observations on a strong line are performed. This to make sure the system works as intended.

### Practical Considerations

There is a slight preference for LO frequency multiples of 8.2–8.1 MHz to cancel out standing waves between the cabin and the secondary. However, we have not seen any problems with this type of ripple during testing. The

(Frequency Switching, continued on page 15)

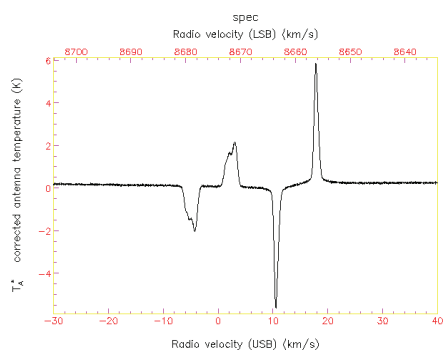


Figure 1. — A frequency switched HARP map of a dark cloud that has been spatially averaged generating very high S/N. The right line is atmospheric CO. Note the wide pressure-broadened shoulder on the atmospheric CO line.

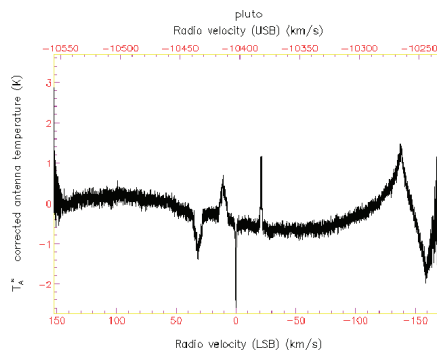


Figure 2. — A long frequency switched spectrum obtained on Pluto. From left to right it shows spectral features due to Galactic CO, atmospheric CO, and ozone.

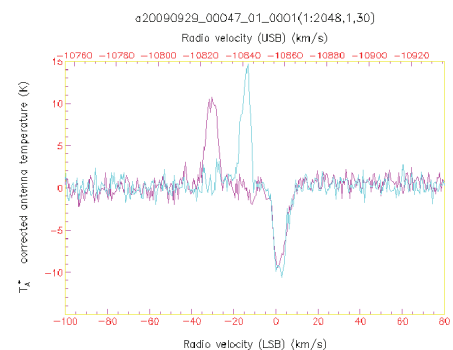


Figure 3. — The blue spectrum is the first spectra in a sequence with RxA. The separation between the negative and positive lines is only half the expected value since RxA has not had time to shift the frequency before the start of the integration.

(Frequency Switching, continued from page 14)

maximum switch is receiver- and frequency-dependent. Failure has occurred for switches of ~40 MHz. We have not found any failures with switches up to 32 MHz which should therefore be a safe switch distance upper limit.

In the OT frequency switching can be combined with jiggle or sample observations. Just set the switch mode to fast frequency switching and the required frequency switch amount. The default switching time is 0.5 Hz (1 s per frequency setting). There is no real advantage in switching faster and this rate helps RxA. For RxA the integration time per point should be as long as possible.

*Examples*

Figure 2 shows a long integration with RxA using frequency switching at the CO line. This is the raw non-post-processed spectrum. The target line is not seen in this spectrum but one can see from left to right a Galactic CO line, a terrestrial atmospheric line, and an ozone line in the other sideband. This illustrates that using frequency switching can be complicated. When observing CO the atmospheric line is a potential problem. There are also many ozone lines that cause unexpected features in the data. These lines are normally switched away when position switching. However, ozone lines occasionally generate spectral features in position switched data. There is also a sinusoidal baseline due to the frequency switching.

Figure 3 shows two individual 2 s RxA spectra from the start of a sequence. This shows the failure of RxA to properly switch at the start of a sequence. The blue spectrum is the first spectrum in the sequence while the red is the second. In the first spectrum RxA is still at the unshifted frequency for the first second and thus the separation between the lines is only half of the expected value. The RxA engineering screen also has to be monitored closely during frequency switching to detect any lock issues. If there are lock issues they may often show up as large DC offsets in the spectrum.

Figure 4 shows an example from HARP. HARP is generally well-behaved when frequency switching. It has none of the problems with timing as with RxA and it will report any locking problem directly and halt the observation. This is a relatively well-behaved baseline — the baselines can be worse when a receptor is misbehaving. Figure 5 shows the same spectrum as in Figure 1 but will the full spectral extent.

*Post-Processing*

A script has been developed to post-process spectra to realize the full S/N available. It is available from the JAC. Figure 6 shows a folded spectrum from the dark cloud map in Figures 1 and 5. Each positive line now has two negative half-intensity counterparts. The baseline is very flat after the folding and the broad shoulder on the atmospheric line is apparent. Note that one of the negative counterparts to the Galactic and atmospheric CO lines now overlaps. Overlap problems of this kind can be troublesome if they affect the positive line. Overlap can depend on the time of year. Furthermore, in crowded line sources it severely limits the use of frequency switching. In principle the lines could be modelled to allow removal of the negative counterparts. The JAC has not developed such a procedure.

The summit pipeline produces spectra that are not post-processed to allow easier diagnosis of unexpected line mixtures and baselines. The plan is for the CADC to have the post-processed spectra available for download. ●

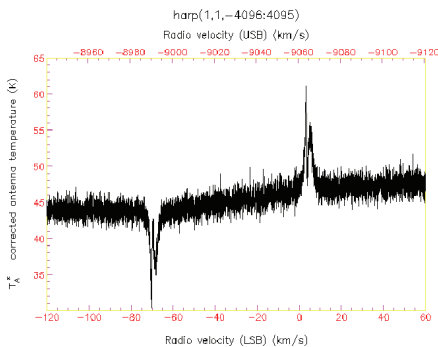


Figure 4. — An example of a HARP frequency switched observation — this is <sup>13</sup>CO so there is no noticeable atmospheric line and there is no ozone line nearby. A slight sinusoidal baseline is present.

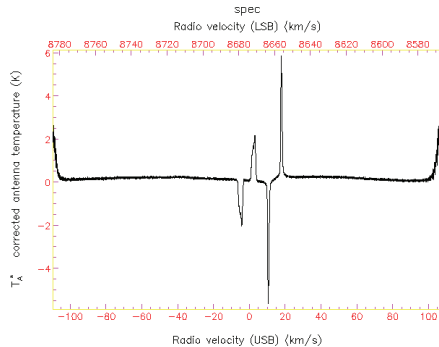


Figure 5. — The same as Figure 1, but showing the complete frequency range.

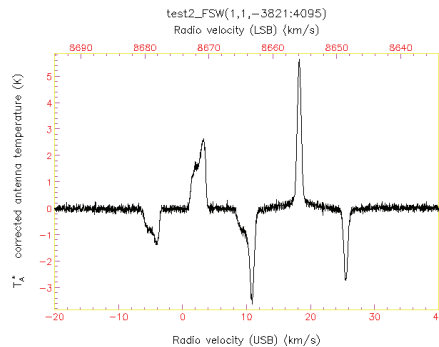
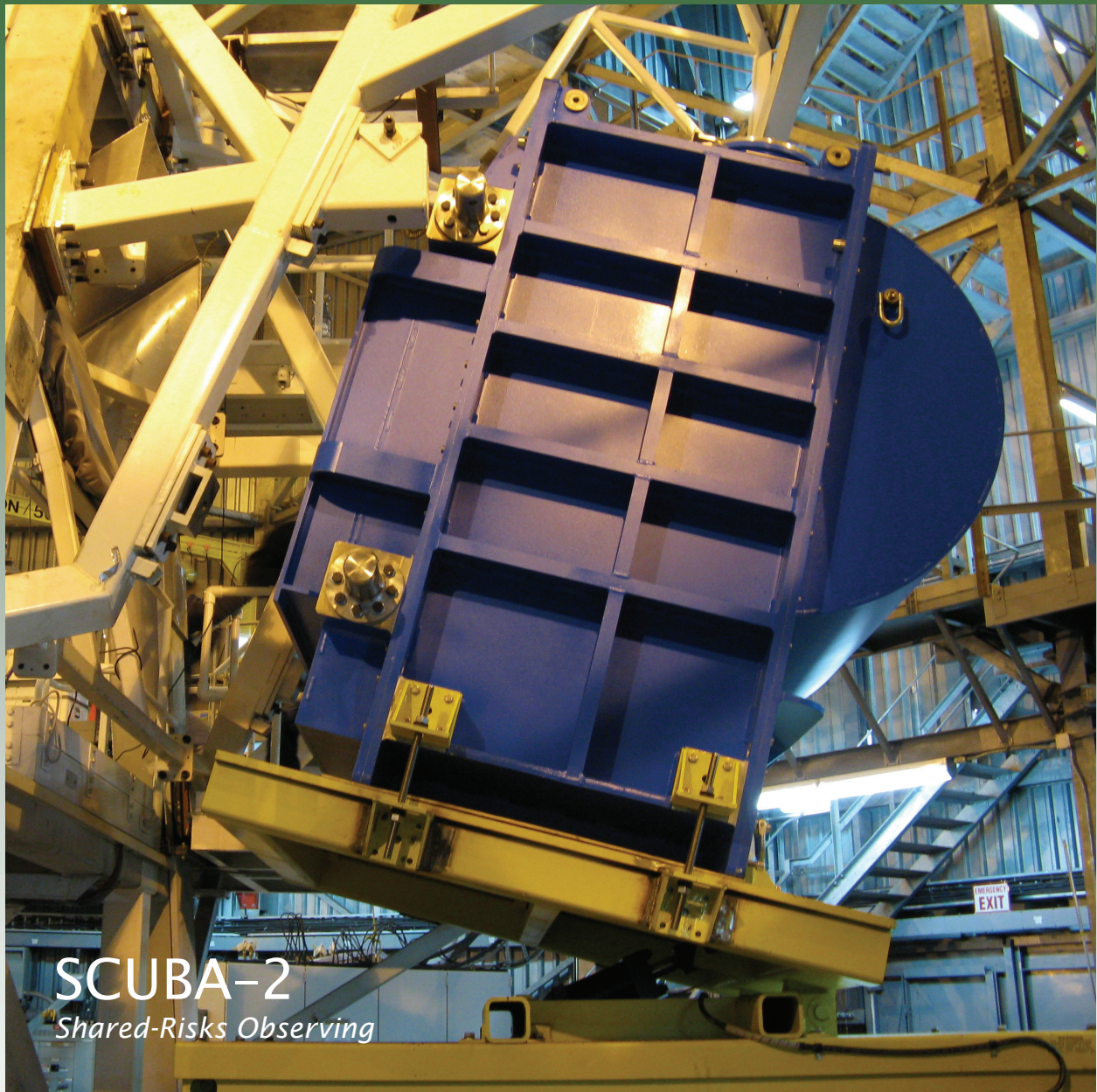


Figure 6. — A folded spectrum from the dark cloud map in Figure 1 and 5.





SCUBA-2  
*Shared-Risks Observing*